Article:
Aalbers, J., Akerib, D.S., Al Musalhi, A.K. et al. (2024) Probing the scalar WIMP-pion coupling with the first LUX-ZEPLIN data. Communications Physics, 7 (1). 292. ISSN: 2399-3650

https://doi.org/10.1038/s42005-024-01774-8

communications physics

Article

https://doi.org/10.1038/s42005-024-01774-8

Probing the scalar WIMP-pion coupling with the first LUX-ZEPLIN data

Check for updates

LZ Collaboration*

Weakly interacting massive particles (WIMPs) may interact with a virtual pion that is exchanged between nucleons. This interaction channel is important to consider in models where the spin-independent isoscalar channel is suppressed. Using data from the first science run of the LUX-ZEPLIN dark matter experiment, containing 60 live days of data in a 5.5 tonne fiducial mass of liquid xenon, we report the results on a search for WIMP-pion interactions. We observe no significant excess and set an upper limit of 1.5×10^{-46} cm^2 at a 90% confidence level for a WIMP mass of 33 GeV/c^2 for this interaction.

Astrophysical and cosmological evidence suggests that roughly 27% of the energy density of the universe is composed of nonluminous dark matter (DM)[1–3]. One of the most popular candidates for DM is the weakly interacting massive particle (WIMP). Various extensions to the Standard Model (SM) naturally give rise to WIMPs making searches for them well motivated[4,5]. Direct dark matter experiments, such as LUX-ZEPLIN (LZ)[6], XENONnT[7], PandaX[8], DEAP-3600[9], and DarkSide-50[10], focus primarily on searching for spin-independent (SI) and spin-dependent (SD) interactions between SM particles and WIMPs with masses in the range of a few GeV/c^2 to several TeV/c^2. Recent results from both LZ[11] and XENONnT[7] place stringent limits on these interactions. In addition to the isoscalar SI channel, the SD channel represents one of the sub-leading non-relativistic effective field theory (NREFT) operators; recent LZ results use the null results to place constraints in the NREFT channels[12].

Expanding from NREFT, chiral effective field theory (ChEFT) admits a new class of next-to-leading-order (NLO) contributions, called two-body currents. One of those two-body currents is the WIMP-pion coupling[13]. WIMP-pion coupling introduces a new structure factor, allowing the study of this channel exclusively, such as was done by XENON1T[14].

In this article, we present the search results for the SI WIMP-pion interaction, using data from the first science run of the LZ experiment. We find no significant evidence of an excess of events above the backgrounds and report an upper limit of 1.5×10^{-46} cm^2 on the process for a 33 GeV/c^2 WIMP at a 90% confidence level.

Results

Chiral effective field theory

In a typical analysis of WIMP search data, the WIMP-nucleon scattering is decomposed into the SI channel, where the interaction searched for is assumed to be isoscalar, and the SD channel, where the interaction searched for is with protons or neutrons only. The SI channel usually emerges as the dominant channel due to its scaling with the square of the number of nucleons[15]. However, neither of these interaction descriptions contain all contributions to their respective channels. It is therefore beneficial to describe the interaction through the lens of an EFT, where additional contributions can be considered. When using a ChEFT Lagrangian to describe the scattering of a WIMP with a nucleus (detailed in Methods), there is a single diagram at leading order (LO), namely the tree-level $\chi N \to \chi N$ (Fig. 1a), where N is the nucleon in the nucleus and χ represents the WIMP. This LO contribution is included in the standard SI channel. At NLO, there are two one-loop diagrams for the single-nucleon process $\chi N \to \chi N$ (Fig. 1b, c), and one diagram for the two-nucleon process $\chi N_1 N_2 \to \chi N_1 N_2$ (Fig. 1d). In the latter case, the two nucleons exchange a meson (dominantly pions in this energy range), and the WIMP couples to this meson. From the perspective of ChEFT, the NLO diagrams need to be included in both the SI and SD channels. Including the two one-loop diagrams change the Wilson coefficients in the standard SI channel whilst the two-body current introduces a new term as a form factor that involves the WIMP-pion vertex. In the SD channel, only the Wilson coefficients are affected. Explicitly, the differential cross-section for the momentum transfer $q = |\vec{q}|$ between the WIMP and the nucleus becomes[16]:

$$\frac{d\sigma_{\chi N}}{dq^2} = \frac{1}{4\pi v^2}\left|c_+ F_+(q^2) + c_- F_-(q^2) + c_\pi F_\pi(q^2)\right|^2 + \frac{1}{v^2(2J+1)}\left(|a_+|^2 S_{00}(q^2) + Re(a_+ a_-^\star) S_{01}(q^2) + |a_-|^2 S_{11}(q^2)\right) \quad (1)$$

where the first term represents the SI channel cross-section $\frac{d\sigma^{SI}_{\chi N}}{dq^2}$, inclusive of the NLO contributions, and the second term corresponds to the SD channel $\frac{d\sigma^{SD}_{\chi N}}{dq^2}$. F and S are the form factors for SI and SD scattering, respectively. v represents the velocity of the WIMP in the laboratory frame and J denotes the nuclear spin. The coefficients c_i and a_i are undetermined constants

*A list of authors and their affiliations appears at the end of the paper. e-mail: bboxer@ucdavis.edu; sam.eriksen@bristol.ac.uk; yqie2@u.rochester.edu

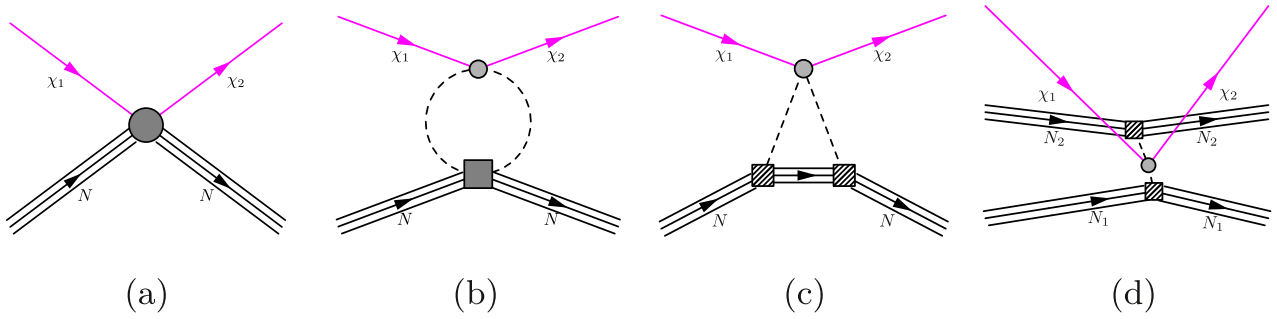

Fig. 1 | Feynman diagrams for WIMP-nucleon scattering described by the ChEFT. a The LO contribution. The black line represents the nucleon and the magenta line represents the WIMP. The large grey circle denotes the WIMP-nucleon vertex. **b**, **c** The one-loop corrections at NLO. The black dashed line represents the pion loop. The grey circle denotes the WIMP-pion vertex, and the hatched square indicates the pion-nucleon 3-vertex and 4-vertex. **d** The two-body current correction at NLO. The dashed line represents the exchanged pion with which the WIMP will interact with.

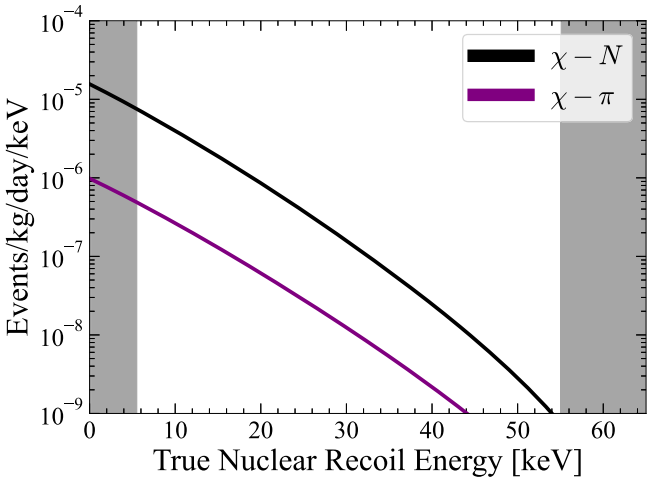

Fig. 2 | Comparison of WIMP-nucleon and WIMP-pion recoil spectra. Differential recoil spectra for isoscalar SI WIMP-nucleon without any NLO correction (black) and SI WIMP-pion (purple) for a WIMP mass of 30 GeV/c^2 on natural xenon. The cross section at zero-momentum σ_0 was set to 10^{-46} cm^2 for both spectra for illustration. The grey regions indicate energy ranges at which signal efficiency falls below 50%. The efficiency is assessed using AmLi and tritium calibration data, discussed in Methods.

Table 1 | The expected and fitted numbers of events from various sources in the 60 d × 5.5 t exposure

Source	Expected events	Fit result
β decays + Det. ER	215 ± 36	222 ± 16
ν ER	27.1 ± 1.6	27.2 ± 1.6
^{127}Xe	9.2 ± 0.8	9.3 ± 0.8
^{124}Xe	5.0 ± 1.4	5.2 ± 1.4
^{136}Xe	15.1 ± 2.4	15.2 ± 2.4
^{8}B CEνNS	0.14 ± 0.01	0.14 ± 0.01
Accidentals	1.2 ± 0.3	1.2 ± 0.3
Subtotal	273 ± 36	280 ± 16
^{37}Ar	[0, 288]	$52.5^{+9.6}_{-8.9}$
Detector neutrons	$0.0^{+0.2}$	$0.0^{+0.2}$
30 GeV/c^2 WIMP	–	$0.0^{+0.6}$
Total	–	333 ± 17

The middle column contains the predicted number of events with uncertainties as described in the text. These uncertainties are used as constraints in a combined fit of the background model and 30 GeV/c^2 WIMP to the data. The result of the fit is shown in the right column. Where the fit result values are zero, no lower uncertainty is set due to the physical boundary.

that will be established through new physics models. The subscripts $+/-$ represent the isoscalar/isovector terms, and the subscript π signifies the process involving the WIMP-pion coupling.

In Eq. (1), the SI channel remains dominant over the SD channel because it has the same scaling as the standard SI cross-section, up to some power of $m_\pi/\Lambda_{\rm QCD}$ and $m_N/\Lambda_{\rm QCD}$. Here m_π and m_N are the masses for the pion and the nucleon respectively, and $\Lambda_{\rm QCD}$ is the non-perturbative scale in QCD. The SI WIMP-pion coupling is dominant over the SD WIMP-nucleon interaction[14].

In this analysis, we examine the SI WIMP-pion coupling term only (Fig. 1d) and set all other coefficients to zero. The WIMP-pion coupling becomes the most relevant in scenarios where the WIMP-nucleon contribution to the SI coupling is suppressed, such as in the minimal supersymmetric standard model[17]. The cross-section is then:

$$\frac{d\sigma^{SI}_{\chi N}}{dq^2} \supset \frac{|c_\pi|^2}{4\pi v^2}|F_\pi(q^2)|^2 = \frac{\sigma^{\rm scalar}_{\chi\pi}}{\mu_\pi^2 v^2}|F_\pi(q^2)|^2, \quad (2)$$

where the WIMP-pion cross section is $\sigma^{\rm scalar}_{\chi\pi} = \frac{\mu_\pi^2}{4\pi}|c_\pi|^2$, with μ_π denoting the WIMP-pion reduced mass.

The differential recoil spectrum for this interaction is then given by[18]:

$$\frac{dR}{dE_r} = \frac{2\rho\sigma^{\rm scalar}_{\chi\pi}}{m_\chi \mu_\pi^2}|F_\pi(q^2)|^2 \int_{v_{\rm min}}^{\infty} \frac{f(\vec{v},t)}{v} d^3v, \quad (3)$$

where E_r represents the recoil energy, and m_χ is the WIMP mass. ρ is the local dark matter density, $f(\vec{v},t)$ is the velocity distribution of dark matter, and $|F_\pi|^2$ is the form factor.

To constrain the SI WIMP-pion coupling, data from the first science run (SR1) of the LUX-ZEPLIN (LZ) experiment are used[11]. The recoil spectra for a SI WIMP-pion interaction with natural xenon, shown in Fig. 2 along with the spectra from an isoscalar SI WIMP-nucleon interaction without any NLO correction, highlight that both interaction channels produce similar falling exponential spectra. The similarity in shape between the WIMP-pion and WIMP-nucleon interactions indicates that the same energy window and data selection used in the LZ SR1 SI analysis can be applied here.

LUX-ZEPLIN detector

The LZ experiment is a low-background, dual-phase time projection chamber (TPC) containing 7 tonnes of liquid xenon (LXe), located in the Davis Campus of the Sanford Underground Research Facility (SURF), South Dakota, USA. An energy deposit in the LXe volume produces scintillation photons and ionisation electrons. The scintillation light from the

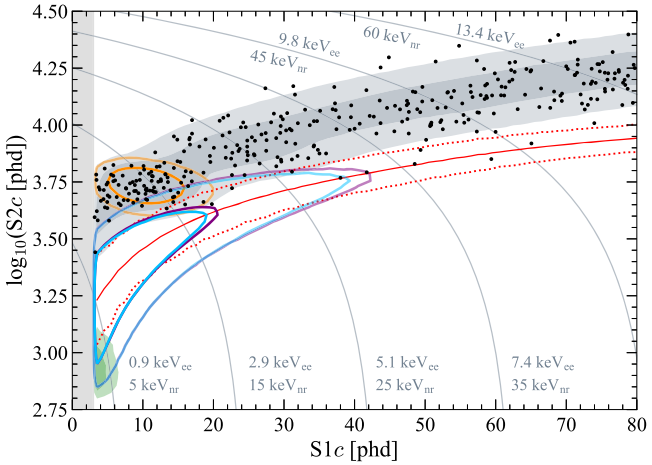

Fig. 3 | The WIMP search data with background and signal models. The black points show the WIMP search data after all cuts in {S1c, log$_{10}$(S2c)} space. The contours that enclose 1σ (dark) and 2σ (light) regions represent the following background models: the shaded grey region indicates the best-fit background model, the orange region indicates ^{37}Ar, and the green region indicates the ^{8}B solar neutrinos. The model for a 30 GeV/c^2 WIMP is shown for both an SI WIMP-pion interaction (purple) and an SI WIMP-nucleon interaction (blue). The solid red line corresponds to the NR median, while the red dotted lines represent the 10–90% percentiles of the expected response.

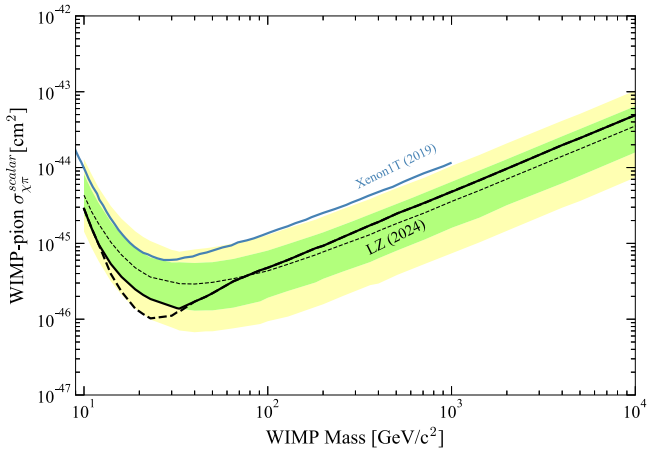

Fig. 4 | Constraints on the SI WIMP-pion interaction cross-section. The solid black line shows the 90% confidence limit of the cross-section for SI WIMP-pion interaction. The black dashed line shows the limit before the power constraint. The black dotted line shows the median of the sensitivity projection, and the green and yellow bands correspond to the 1σ and 2σ sensitivity bands, respectively. In blue are the WIMP-pion results from XENON1T[14].

initial interaction is promptly detected (S1) by an array of photomultiplier tubes (PMTs). An electric field, applied across the detector volume, drifts the liberated electrons to the liquid-gas interface. These electrons are extracted into the xenon gas and are accelerated, producing proportional scintillation and a secondary light signal (S2). The S1:S2 ratio differs for electronic recoils (ERs) and nuclear recoils (NRs), allowing for discrimination between interaction types. A correction applied to the S1 and S2 observables (S1c and S2c, respectively) accounts for the fact that the response of the detector varies as a function of the interaction position. Additional details of the experiment, and run conditions during data collection, can be found in Methods.

First science run analysis

The SR1 data, collected between December 2021 and May 2022, contain a total of 60 live days of exposure. The fiducial volume (FV) used in this analysis is 5.5 ± 0.2 tonnes. Vertically, the FV captures events with a drift time between 86 µs and 936.5 µs, which corresponds to 12.8 cm from the gate electrode and 2.2 cm from the cathode electrode. The FV extends radially to 5.2 cm from the TPC wall for events with drift time <200 µs, 5.0 cm for drift time >800 µs, and 4.0 cm everywhere else. The signal region of interest (ROI) is defined as S1c in the range of 3–80 photons detected (phd), S2 greater than 600 phd and S2c less than 10^5 phd. A series of selection criteria are applied to the data to remove uncharacteristic detector behaviour and WIMP-like backgrounds, leaving 335 events in the final data set[11].

The expected background contributions in the ROI are given in Table 1. The ER backgrounds are dominated by radioactive decays in the xenon from ^{222}Rn, ^{220}Rn, ^{85}Kr and ^{136}Xe, as well as interactions from solar neutrinos. Subdominant backgrounds come from other radioactive impurities in the xenon and detector materials. The NR backgrounds are from ^{8}B coherent neutrino-nuclear scattering and neutrons emitted from detector materials. Events caused by accidental coincidences of unrelated S1 and S2 pulses are also included in the background model. Detailed compositions of each background are discussed in Methods. Figure 3 shows the data set, as well as backgrounds and the signal distribution for a 30 GeV/c^2 WIMP through the SI WIMP-pion interaction. Also shown is the signal distribution for an interaction through the isoscalar SI WIMP-nucleon channel. For any given WIMP mass, an interaction through the WIMP-pion channel will spread over a more extended range in {S1c, log$_{10}$(S2c)} than an interaction through the WIMP-nucleon channel. This can be explained by comparing the recoil spectra in Fig. 2. Within the ROI, the gradient of the recoil spectrum of the WIMP-pion coupling is smaller than that of the WIMP-nucleon coupling, causing the WIMP-pion signal to reach the 1σ and 2σ levels at higher recoil energies. Although this effect is very small, it may be possible to discriminate between the SI WIMP-nucleon and SI WIMP-pion interactions[19].

WIMP masses between 9 GeV/c^2 and 10,000 GeV/c^2 are tested with a frequentist statistical analysis described in Methods and no excess of events above backgrounds are observed at any WIMP mass. Shown in Fig. 4 are the limits on the SI WIMP-pion interaction cross-section, as determined by LZ, together with a previous result from XENON1T[14]. A power constraint is applied to restrict the upper limit from falling 1σ below the median expectation from the background-only hypothesis at low energies, such that the probability of excluding a given WIMP-pion cross section if the background-only hypothesis is true does not fall below 16%[11,20,21]. This effect is visible in the 10–20 GeV/c^2 mass range. The 90% confidence level upper limit has a minimum of 1.5×10^{-46} cm^2 for a 33 GeV/c^2 WIMP.

At all masses, the best-fit number of events is 333 ± 17 events, compared to the 335 in the dataset. The data are compared to the best-fit background model in a reconstructed energy projection, using an unbinned Kolmogorov–Smirnov test, which results in a p-value of 0.96. The predicted and best-fit background composition are shown in Table 1. The background rates and the p-value are similar to the results in the LZ SI WIMP-nucleon analysis[11].

Methods

Detector description

Both the LZ experiment and the detector conditions for these data have previously been described in detail[6,11]. In this section, the information relevant to this work is summarised.

At the core of the LZ experiment is a cylindrical TPC (described in Results), ~1.5 m in both height and diameter, containing 7 tonnes of LXe in the active volume. The TPC is equipped with a total of 494 3-inch PMTs, located at the top and bottom of the TPC to detect scintillation light. The sensitive volume of the LZ experiment is supported by two veto detectors: a xenon "Skin" veto surrounding the active mass, and a near-hermetic "outer detector" (OD) consisting of acrylic tanks containing 17 tonnes of gadolinium-loaded liquid scintillator (0.1% by mass), and surrounded by 238 tonnes of ultra-pure water. The Skin detector is designed to identify multiple scattering interactions entering or exiting the TPC and is outfitted with 93 1-inch and 38 2-inch PMTs. The OD is designed to capture and

identify neutrons that may scatter in the TPC and is equipped with 120 8-inch PMTs.

The light detected in the TPC (S1 and S2), once position corrected, can be correlated to the number of photons and electrons produced (n_{ph} and n_e), by linear scaling factors, g_1 and g_2:

$$\mathrm{S1\,c} = \mathrm{g_1}\langle \mathrm{n_{ph}}\rangle;\ \mathrm{S2\,c} = \mathrm{g_2}\langle \mathrm{n_e}\rangle. \tag{4}$$

The energy reconstruction of several monoenergetic peaks from background and calibration ER sources are used to determine $g_1 = 0.114 \pm 0.002$ phd/photon and $g_2 = 47.1 \pm 1.1$ phd/electron.

The ER and NR responses of the TPC detector are measured using dedicated in-situ calibrations with tritiated methane (0–18.6 keV ERs) and D-D fusion neutrons (0–74 keV NRs). The detector and model response parameters from NEST 2.3.7 (Noble Element Simulation Technique)[22,23] are tuned to the ER and NR calibration data to reproduce the observed data. The ER model parameters are propagated into the NR model which is in agreement of better than 1% for the band medians when compared to DD calibration data. The discrimination between ERs and NRs is 99.9% below a flat nuclear recoil band median[23].

TPC single-scatter events with coincident activity in the Skin or OD are removed to reduce backgrounds. OD and Skin events within ±0.3 µs and ±0.5 µs of the TPC S1, respectively, are removed to mitigate γ-rays. Neutrons, which can be captured on hydrogen and gadolinium in the OD, can be tagged by the Skin and OD. OD pulses greater than 200 keV within 1200 µs after the TPC S1, and large Skin pulses within the same time window are removed. The neutron tagging efficiency for TPC single scatters was determined using AmLi calibration sources placed at nine locations close to the TPC. The position-averaged efficiency of tagging TPC events in the nuclear recoil band is measured as 89 ± 3%. The false veto rate, determined from background data, is measured as 5%.

Background composition

The backgrounds in these data have previously been described[24], as such only a minimal description is given here.

The ER backgrounds are dominated by radioactive impurities dispersed in the LXe. These are ^{214}Pb from the ^{222}Rn decay chain, ^{212}Pb from the ^{220}Rn decay chain, and ^{85}Kr. Peaks in respective decay chains outside of the ROI are used to constrain the rate of ^{214}Pb and ^{212}Pb. The concentration of ^{85}Kr is measured with a liquid nitrogen cold trap, and its rate is further validated n situ by counting coincident β-γ-ray decays[24]. All of these components have a near-flat energy spectrum in the ROI and are summed together into the β decays background component. These are considered together with the near-flat contribution from γ-rays which originate from detector materials and the cavern in which the detector resides[25,26]. Solar neutrinos, also a near-flat contribution in the ROI, are kept separate as the prediction on the event rate is very precise[20,27–29]. ^{124}Xe, a double electron capture, and ^{136}Xe, a double β decay, are naturally occurring isotopes, of which the contributions are predicted from known isotopic abundances and decay schemes[30–32]. Two ER backgrounds are present in this dataset as a result of cosmogenic activation of the xenon prior to arrival at SURF. Both ^{127}Xe and ^{37}Ar are expected to only contribute significantly to this first science-run dataset. The rate of ^{37}Ar is estimated from the length of time the xenon was exposed to cosmic rays on the surface[33], and ^{127}Xe by K-shell de-excitations and Skin-tagging efficiency for γ-rays[11].

The NR backgrounds are comprised of neutrons emitted from radioactive detector materials, through (α,n) reactions and spontaneous fission, and from coherent elastic neutrino-nucleus scattering. The rate of radiogenic neutrons is constrained by the rate of events tagged by the OD veto detector. The contribution of ^{8}B solar neutrinos is calculated from the known solar flux[27]. Finally, isolated S1 and S2 pulses can appear within the same event window, appearing as a single-scatter-like event. The rate of these accidentals is constrained by sideband samples of single-scatter-like events.

Models for these backgrounds in $\{S1_c, \log_{10}(S2_c)\}$ are produced using BACCARAT, a package based on GEANT4[34,35], together with a detector model, which is fine-tuned using the NEST detector model. The header file for NEST 2.3.7 that will reproduce the ER and NR response models used in this analysis is available[11].

ChEFT Lagrangian

The ChEFT used in this analysis begins as a minimal extension to the SM to accommodate interactions between WIMPs and nucleons. This is introduced via the the following Lagrangian[13,16]:

$$\begin{aligned}\mathscr{L}_{\mathrm{full}} = &\mathscr{L}_{\mathrm{QCD}} \\ &+ \frac{1}{\Lambda^2}\sum_{q=u,d,s,c,b,t}\left[\lambda_q^V \bar{\chi}\gamma^\mu\chi\bar{q}\gamma_\mu q + \lambda_q^A \bar{\chi}\gamma^\mu\gamma_5\chi\bar{q}\gamma_\mu\gamma_5 q\right] \\ &+ \frac{1}{\Lambda^3}\sum_{q=u,d,s,c,b,t}\left[m_q\lambda_q^S\bar{\chi}\chi\bar{q}q + \lambda_G\frac{\alpha_s}{\pi}\bar{\chi}\chi\,\mathrm{Tr}\left(\mathrm{G}_{\mu\nu}\mathrm{G}^{\mu\nu}\right)\right]\end{aligned} \tag{5}$$

where χ, q, $G_{\mu\nu}$ represent the fermionic WIMP, quark, and gauge fields respectively. m_q is quark mass, α_s is the strong coupling constant, and Λ is the new physics scale. The first new term is dimension-6 and can be decomposed into a vector interaction and an axial-vector interaction. The second new term is dimension-7, corresponding to the scalar interaction. The λ_q with superscripts is the coupling constant for each interaction.

The full theory Lagrangian shown in Eq. (5) works for any energy scale, including low-energy WIMP-nucleon scattering relevant to LZ WIMP-search, its computation is impractically complicated. For convenience, in this analysis we use an EFT for the low-energy dynamics[13,16,36,37]. Given the chiral EFT Lagrangian, we are able to write down the Feynman diagrams in Fig. 1.

Recoil spectrum

In this analysis, recoil spectra are generated using ChiralEFT4DM[38]. The parameters used in the spectra generation follow the direct dark matter search conventions[20], where the dark matter density $\rho = 0.3$ GeV/cm^3[18], and the velocity distribution is described by the Standard Halo Model with $\vec{v}_\circledast$ = (11.1, 12.2, 7.3) km/s (solar peculiar velocity)[39], $\vec{v}_0$ = (0, 238, 0) km/s (local standard of rest velocity)[40,41] and $v_{\mathrm{esc}} = 544$ km/s (galactic escape speed)[42]. For a zero-momentum scalar SI WIMP-pion cross-section, $\sigma^{scalar}_{\chi\pi,0}$, a value of 10^{-46} cm^2 was used; based on constraints from XENON1T[14]. The xenon target is considered as a mixture of xenon isotopes weighted by their natural abundances. The form factor uses generalised two-body structure factors[16] on xenon shell-model calculations[43–45].

Statistical method

A hypothesis test is performed to evaluate the consistency of the observed data with the presence of WIMPs interacting through the SI WIMP-pion channel. The test statistic utilised for assessing the Parameter of Interest (POI) is defined as a negative log-likelihood, $q = -2\ln(\lambda)$. Here, λ represents the Profile Likelihood Ratio (PLR), defined as:

$$\lambda(\mu) = \frac{\mathscr{L}(\mu, \hat{\hat{\theta}})}{\mathscr{L}(\hat{\mu}, \hat{\theta})}, \tag{6}$$

where μ is the POI, taken to be the number of WIMP-pion scatterings, and θ represents a set of nuisance parameters related to the contribution of individual background components to the overall observed number of events. Variables marked with hats represent parameters that maximise the likelihood globally, while those marked with double hats maximise the likelihood for a fixed POI.

For this analysis, an extended unbinned two-sided likelihood fit to the search data in $\{S1_c, \log_{10}(S2_c)\}$ is performed[20]. The observable space (x_e) is then in 2D with $\{S1_c, \log_{10}(S2_c)\}$.

The likelihood function, $\mathscr{L}$, is defined as:

$$\begin{aligned}\mathscr{L}(\theta) =& \text{Poisson}(N_0|\mu_{\text{tot}}) \\ &\times \prod_{e=1}^{N_0} \frac{1}{\mu_{\text{tot}}} \left(\mu_s f_s(x_e) + \sum_{b=1}^{N_b} \mu_b f_b(x_e) \right) \\ &\times \prod_{b=1}^{N_b} g_b(\mu_b|\nu_b).\end{aligned} \tag{7}$$

The function accounts for Poisson statistics of the observed counts (N_0) and the expected number of events (μ_{tot}); which is the sum of the expected number of signal (μ_s) and background (μ_b) events which is a function of θ. In the summation, N_b is the number of probability density functions of the backgrounds. Signal and background components are incorporated as functions of the observable parameter (x_e), via the inclusion of $f_s(x_e)$ and $f_b(x_e)$, respectively. $g_b(\mu_b|\nu_b)$ represents constraint functions on the rate of each background, typically Gaussian distributions with widths defined by the uncertainties of the backgrounds.

A probability density function in observable space is produced for each background and signal under test. To simulate the background and signal components, the BACCARAT package based on GEANT4[34,35] is utilised, along with a bespoke simulation of the LZ detector response. As part of this methodology, the uncertainties associated with the background components are included as constraint terms in a combined fit of the background model to the data. The PLR calculation is executed using the LZStats codebase[46].

Background fluctuations can lead to downward fluctuations in the observed limit. To protect against this, a power constraint is introduced to not allow the limit to exclude models where the rejection power of the alternate hypothesis is less than $\pi_{\text{crit}} = 0.16$[20,21]. This restricts the observed limit to not fall below 1σ from the median expected limit.

Data availability

The data points associated with the limit curve (Fig. 4) can be found at https://www.hepdata.net/record/152755. The WIMP search data (Fig. 3) and efficiency curve (not shown in paper) can be found at https://www.hepdata.net/record/ins2107834. Additional data is available from the corresponding author upon request.

Received: 5 June 2024; Accepted: 9 August 2024;
Published online: 31 August 2024

References

1. Sofue, Y. & Rubin, V. Rotation curves of spiral galaxies. *Annu. Rev. Astron. Astrophys.* **39**, 137–174 (2001).
2. Arbey, A. & Mahmoudi, F. Dark matter and the early universe: a review. *Prog. Part. Nucl. Phys.* **119**, 103865 (2021).
3. Bertone, G. & Hooper, D. History of dark matter. *Rev. Mod. Phys.* **90**, 045002 (2018).
4. Akerib, D. S. et al. Snowmass2021 cosmic frontier dark matter direct detection to the neutrino fog. Preprint at https://arxiv.org/abs/2203.08084 (2022).
5. Billard, J. et al. Direct detection of dark matter-APPEC committee report. *Rep. Prog. Phys.* **85**, 056201 (2022).
6. Akerib, D. S. et al. The LUX-ZEPLIN (LZ) experiment. *Nucl. Instrum. Methods Phys. Res. Sect. A* **953**, 163047 (2020).
7. Aprile, E. et al. First dark matter search with nuclear recoils from the XENONnT experiment. *Phys. Rev. Lett.* **131**, 041003 (2023).
8. Meng, Y. et al. Dark matter search results from the PandaX-4T commissioning run. *Phys. Rev. Lett.* **127**, 261802 (2021).
9. Adhikari, P. et al. Constraints on dark matter-nucleon effective couplings in the presence of kinematically distinct halo substructures using the DEAP-3600 detector. *Phys. Rev. D* **102**, 082001 (2020).
10. Agnes, P. et al. Effective field theory interactions for liquid argon target in DarkSide-50 experiment. *Phys. Rev. D* **101**, 062002 (2020).
11. Aalbers, J. et al. First dark matter search results from the LUX-ZEPLIN (LZ) experiment. *Phys. Rev. Lett.* **131**, 041002 (2023).
12. Aalbers, J. et al. First constraints on WIMP-nucleon effective field theory couplings in an extended energy region from LUX-ZEPLIN. *Phys. Rev. D* **109**, 092003 (2024).
13. Cirigliano, V., Graesser, M. L. & Ovanesyan, G. WIMP-nucleus scattering in chiral effective theory. *J. High Energy Phys.* **2012**, 25 (2012).
14. Aprile, E. et al. First results on the scalar WIMP-Pion coupling, Using the XENON1T experiment. *Phys. Rev. Lett.* **122**, 071301 (2019).
15. Engel, J., Pittel, S. & Vogel, P. Nuclear physics of dark matter detection. *Int. J. Mod. Phys. E* **01**, 1–37 (1992).
16. Hoferichter, M., Klos, P., Menéndez, J. & Schwenk, A. Analysis strategies for general spin-independent WIMP-nucleus scattering. *Phys. Rev. D* **94**, 063505 (2016).
17. Crivellin, A., Hoferichter, M., Procura, M. & Tunstall, L. C. Light stops, blind spots, and isospin violation in the mssm. *J. High Energy Phys.* **2015**, 129 (2015).
18. Lewin, J. & Smith, P. Review of mathematics, numerical factors, and corrections for dark matter experiments based on elastic nuclear recoil. *Astropart. Phys.* **6**, 87–112 (1996).
19. Fieguth, A. et al. Discriminating wimp-nucleus response functions in present and future xenon-like direct detection experiments. *Phys. Rev. D* **97**, 103532 (2018).
20. Baxter, D. et al. Recommended conventions for reporting results from direct dark matter searches. *Eur. Phys. J. C* **81**, 907 (2021).
21. Cowan, G., Cranmer, K., Gross, E. & Vitells, O. Power-constrained limits. Preprint at https://arxiv.org/abs/1105.3166 (2011).
22. Szydagis, M. et al. Noble element simulation technique https://doi.org/10.5281/zenodo.6534007 (2022).
23. Szydagis, M. et al. A review of NEST models, and their application to improvement of particle identification in liquid xenon experiments. Preprint at https://arxiv.org/abs/2211.10726 (2023).
24. Aalbers, J. et al. Background determination for the LUX-ZEPLIN (LZ) dark matter experiment. *Phys. Rev. D* **108**, 012010 (2023).
25. Akerib, D. et al. The LUX-ZEPLIN (LZ) radioactivity and cleanliness control programs. *Eur. Phys. J. C* **80**, 1044 (2020).
26. Akerib, D. et al. Measurement of the gamma ray background in the Davis cavern at the Sanford Underground Research Facility. *Astropart. Phys.* **116**, 102391 (2020).
27. Agostini, M. et al. Simultaneous precision spectroscopy of *pp*, ^{7}Be, and *pep* solar neutrinos with Borexino Phase-II. *Phys. Rev. D* **100**, 082004 (2019).
28. Aharmim, B. et al. Combined analysis of all three phases of solar neutrino data from the Sudbury Neutrino Observatory. *Phys. Rev. C* **88**, 025501 (2013).
29. Vinyoles, N. et al. A new generation of standard solar models. *Astrophys. J.* **835**, 202 (2017).
30. Berglund, M. & Wieser, M. E. Isotopic compositions of the elements 2009 (IUPAC Technical Report). *Pure Appl. Chem.* **83**, 397–410 (2011).
31. Aprile, E. et al. Observation of two-neutrino double electron capture in ^{124}Xe with XENON1T. *Nature* **568**, 532–535 (2019).
32. Albert, J. B. et al. Improved measurement of the $2\nu\beta\beta$ half-life of ^{136}Xe with the EXO-200 detector. *Phys. Rev. C* **89**, 015502 (2014).
33. Aalbers, J. et al. Cosmogenic production of ^{37}Ar in the context of the LUX-ZEPLIN experiment. *Phys. Rev. D* **105**, 082004 (2022).
34. Akerib, D. et al. Simulations of events for the LUX-ZEPLIN (LZ) dark matter experiment. *Astropart. Phys.* **125**, 102480 (2021).
35. Allison, J. et al. Recent developments in Geant4. *Nucl. Instrum. Methods Phys. Res. Sect. A* **835**, 186–225 (2016).
36. Georgi, H. An effective field theory for heavy quarks at low-energies. *Phys. Lett. B* **240**, 447–450 (1990).
37. Weinberg, S. Effective chiral lagrangians for nucleon-pion interactions and nuclear forces. *Nucl. Phys. B* **363**, 3–18 (1991).

38. Hoferichter, M., Klos, P., Menéndez, J. & Schwenk, A. Analysis strategies for general spin-independent wimp-nucleus scattering. *Phys. Rev. D* **94**, 063505 (2016).
39. Schoenrich, R., Binney, J. & Dehnen, W. Local kinematics and the local standard of rest. *Mon. Not. Roy. Astron. Soc.* **403**, 1829 (2010).
40. Bland-Hawthorn, J. & Gerhard, O. The galaxy in context: structural, kinematic, and integrated properties. *Annu. Rev. Astron. Astrophys* **54**, 529–596 (2016).
41. Abuter, R. et al. Improved GRAVITY astrometric accuracy from modeling optical aberrations. *Astron. Astrophys.* **647**, A59 (2021).
42. Smith, M. C. et al. The RAVE survey: constraining the local galactic escape speed. *Mon. Not. Roy. Astron. Soc.* **379**, 755–772 (2007).
43. Vietze, L., Klos, P., Menéndez, J., Haxton, W. C. & Schwenk, A. Nuclear structure aspects of spin-independent WIMP scattering off xenon. *Phys. Rev. D* **91**, 043520 (2015).
44. Hoferichter, M., Klos, P., Menéndez, J. & Schwenk, A. Nuclear structure factors for general spin-independent WIMP-nucleus scattering. *Phys. Rev. D* **99**, 055031 (2019).
45. Caurier, E., Martinez-Pinedo, G., Nowacki, F., Poves, A. & Zuker, A. P. The Shell model as unified view of nuclear structure. *Rev. Mod. Phys.* **77**, 427–488 (2005).
46. Samblas, I. O. *A statistical framework for the characterisation of WIMP dark matter with the LUX-ZEPLIN experiment*. Ph.D. thesis, Imperial College London https://doi.org/10.25560/76523 (2019).
47. Faulkner, P. et al. GridPP: development of the UK computing Grid for particle physics. *J. Phys. G* **32**, N1 (2005).
48. Britton, D. et al. GridPP: the UK grid for particle physics. *Phil. Trans. R. Soc. A* **367**, 2447–2457 (2009).

Acknowledgements

The research supporting this work took place in part at the Sanford Underground Research Facility (SURF) in Lead, South Dakota. Funding for this work is supported by the U.S. Department of Energy, Office of Science, Office of High Energy Physics under Contract Numbers DE-AC02-05CH11231, DE-SC0020216, DE-SC0012704, DE-SC0010010, DE-AC02-07CH11359, DE-SC0012161, DE-SC0015910, DE-SC0014223, DE-SC0010813, DE-SC0009999, DE-NA0003180, DE-SC0011702, DE-SC0010072, DE-SC0015708, DE-SC0006605, DE-SC0008475, DE-SC0019193, DE-FG02-10ER46709, UW PRJ82AJ, DE-SC0013542, DE-AC02-76SF00515, DE-SC0018982, DE-SC0019066, DE-SC0015535, DE-SC0019319, DE-SC0024225, DE-SC0024114, DE-AC52-07NA27344, & DOE-SC0012447. This research was also supported by U.S. National Science Foundation (NSF); the UKRI's Science & Technology Facilities Council under award numbers ST/M003744/1, ST/M003655/1, ST/M003639/1, ST/M003604/1, ST/M003779/1, ST/M003469/1, ST/M003981/1, ST/N000250/1, ST/N000269/1, ST/N000242/1, ST/N000331/1, ST/N000447/1, ST/N000277/1, ST/N000285/1, ST/S000801/1, ST/S000828/1, ST/S000739/1, ST/S000879/1, ST/S000933/1, ST/S000844/1, ST/S000747/1, ST/S000666/1, ST/R003181/1, ST/W000547/1, ST/W000636/1, ST/W000490/1; Portuguese Foundation for Science and Technology (FCT) under award numbers PTDC/FIS-PAR/2831/2020; the Institute for Basic Science, Korea (budget number IBS-R016-D1); the Swiss National Science Foundation (SNSF) under award number 10001549. This research was supported by the Australian Government through the Australian Research Council Centre of Excellence for Dark Matter Particle Physics under award number CE200100008. We acknowledge additional support from the STFC Boulby Underground Laboratory in the U.K., the GridPP[47,48] and IRIS Collaborations, in particular at Imperial College London and additional support by the University College London (UCL) Cosmoparticle Initiative, and the University of Zurich. We acknowledge additional support from the Center for the Fundamental Physics of the Universe, Brown University. K.T. Lesko acknowledges the support of Brasenose College and Oxford University. The LZ Collaboration acknowledges the key contributions of Dr. Sidney Cahn, Yale University, in the production of calibration sources. This research used resources of the National Energy Research Scientific Computing Center, a DOE Office of Science User Facility supported by the Office of Science of the U.S. Department of Energy under Contract No. DE-AC02-05CH11231. We gratefully acknowledge support from GitLab through its GitLab for Education Program. The University of Edinburgh is a charitable body, registered in Scotland, with the registration number SC005336. The assistance of SURF and its personnel in providing physical access and general logistical and technical support is acknowledged. We acknowledge the South Dakota Governor's office, the South Dakota Community Foundation, the South Dakota State University Foundation, and the University of South Dakota Foundation for use of xenon. We also acknowledge the University of Alabama for providing xenon. For the purpose of open access, the authors have applied a Creative Commons Attribution (CC BY) licence to any Author Accepted Manuscript version arising from this submission.

Author contributions

This work is the result of the contributions and efforts of all participating Institutes of the LZ Collaboration. The collaboration has constructed and operated the LZ apparatus and performed the data processing, calibration, and data selections. Y. Qie initiated the WIMP-pion studies and performed the calculation of theoretical models. S. Eriksen and Y. Qie performed the data analysis and hypothesis tests. S. Eriksen, B. Boxer and Y. Qie prepared the paper draft. The paper was reviewed by A. Kaboth, A. Manalaysay, A. Wang. All authors approved the final version of the manuscript.

Competing interests

M.S. is a Guest Editor for Communications Physics but was not involved in the editorial review of, or the decision to publish this article. All other authors declare no competing interests.

Additional information

Supplementary information The online version contains supplementary material available at https://doi.org/10.1038/s42005-024-01774-8.

Correspondence and requests for materials should be addressed to B. Boxer, S. R. Eriksen or Y. Qie.

Peer review information *Communications Physics* thanks Masayuki Wada, Luca Scotto Lavina and the other, anonymous, reviewer(s) for their contribution to the peer review of this work. A peer review file is available.

LZ Collaboration

J. Aalbers[1,2], D. S. Akerib[1,2], A. K. Al Musalhi[3], F. Alder[3], C. S. Amarasinghe[4,5], A. Ames[1,2], T. J. Anderson[1,2], N. Angelides[6], H. M. Araújo[6], J. E. Armstrong[7], M. Arthurs[1,2], A. Baker[6], S. Balashov[8], J. Bang[9], E. E. Barillier[5,10], J. W. Bargemann[4], K. Beattie[11], T. Benson[12], A. Bhatti[7], A. Biekert[11,13], T. P. Biesiadzinski[1,2], H. J. Birch[5,10], E. J. Bishop[14], G. M. Blockinger[15], B. Boxer[16] ✉, C. A. J. Brew[8], P. Brás[17], S. Burdin[18], M. Buuck[1,2], M. C. Carmona-Benitez[19], M. Carter[18], A. Chawla[20], H. Chen[11], J. J. Cherwinka[12], Y. T. Chin[19], N. I. Chott[21], M. V. Converse[22], A. Cottle[3], G. Cox[3], D. Curran[23], C. E. Dahl[24,25], A. David[3], J. Delgaudio[23], S. Dey[26], L. de Viveiros[19], L. Di Felice[6], C. Ding[9], J. E. Y. Dobson[27], E. Druszkiewicz[22], S. R. Eriksen[28] ✉, A. Fan[1,2], N. M. Fearon[26], N. Fieldhouse[26], S. Fiorucci[11], H. Flaecher[28], E. D. Fraser[18], T. M. A. Fruth[29], R. J. Gaitskell[9], A. Geffre[23], J. Genovesi[21], C. Ghag[3], R. Gibbons[11,13], S. Gokhale[30], J. Green[26], M. G. D. van der Grinten[8], J. J. Haiston[21], C. R. Hall[7], S. Han[1,2], E. Hartigan-O'Connor[9], S. J. Haselschwardt[11], M. A. Hernandez[5,10], S. A. Hertel[31], G. Heuermann[5], G. J. Homenides[32], M. Horn[23], D. Q. Huang[5], D. Hunt[26], E. Jacquet[6], R. S. James[3,41], J. Johnson[16], A. C. Kaboth[20], A. C. Kamaha[33], M. Kannichankandy[15], D. Khaitan[22], A. Khazov[8], I. Khurana[3], Y. D. Kim[34], J. Kim[4], J. Kingston[16], R. Kirk[9], D. Kodroff[11,19], L. Korley[5], E. V. Korolkova[35], H. Kraus[26], S. Kravitz[11,36], L. Kreczko[28], V. A. Kudryavtsev[35], D. S. Leonard[34], K. T. Lesko[11], C. Levy[15], J. Lin[11,13], A. Lindote[17], R. Linehan[1,2], W. H. Lippincott[4], M. I. Lopes[17], W. Lorenzon[5], C. Lu[9], S. Luitz[1], P. A. Majewski[8], A. Manalaysay[11], R. L. Mannino[37], C. Maupin[23], M. E. McCarthy[22], G. McDowell[5], D. N. McKinsey[11,13], J. McLaughlin[24], J. B. McLaughlin[3], R. McMonigle[15], E. H. Miller[1,2], E. Mizrachi[7,37], A. Monte[4], M. E. Monzani[1,2,38], J. D. Morales Mendoza[1,2], E. Morrison[21], B. J. Mount[39], M. Murdy[31], A. St. J. Murphy[14], A. Naylor[35], H. N. Nelson[4], F. Neves[17], A. Nguyen[14], J. A. Nikoleyczik[12], I. Olcina[11,13], K. C. Oliver-Mallory[6], J. Orpwood[35], K. J. Palladino[26], J. Palmer[20], N. J. Pannifer[28], N. Parveen[15], S. J. Patton[11], B. Penning[5,10], G. Pereira[17], E. Perry[3], T. Pershing[37], A. Piepke[32], Y. Qie[22] ✉, J. Reichenbacher[21], C. A. Rhyne[9], Q. Riffard[11], G. R. C. Rischbieter[5,10], H. S. Riyat[14], R. Rosero[30], T. Rushton[35], D. Rynders[23], D. Santone[20], A. B. M. R. Sazzad[32], R. W. Schnee[21], S. Shaw[14], T. Shutt[1,2], J. J. Silk[7], C. Silva[17], G. Sinev[21], J. Siniscalco[3], R. Smith[11,13], V. N. Solovov[17], P. Sorensen[11], J. Soria[11,13], I. Stancu[32], A. Stevens[3,6], K. Stifter[25], B. Suerfu[11,13], T. J. Sumner[6], M. Szydagis[15], W. C. Taylor[9], D. R. Tiedt[23], M. Timalsina[11,21], Z. Tong[6], D. R. Tovey[35], J. Tranter[35], M. Trask[4], M. Tripathi[16], D. R. Tronstad[21], A. Vacheret[6], A. C. Vaitkus[9], O. Valentino[6], V. Velan[11], A. Wang[1,2], J. J. Wang[32], Y. Wang[11,13], J. R. Watson[11,13], R. C. Webb[40], L. Weeldreyer[32], T. J. Whitis[4], M. Williams[5], W. J. Wisniewski[1], F. L. H. Wolfs[22], S. Woodford[18], D. Woodward[11,19], C. J. Wright[28], Q. Xia[11], X. Xiang[9,30], J. Xu[37], M. Yeh[30] & E. A. Zweig[33]

[1]SLAC National Accelerator Laboratory, Menlo Park, CA, USA. [2]Kavli Institute for Particle Astrophysics and Cosmology, Stanford University, Stanford, CA, USA. [3]Department of Physics and Astronomy, University College London (UCL), London, UK. [4]Department of Physics, University of California, Santa Barbara, Santa Barbara, CA, USA. [5]University of Michigan, Randall Laboratory of Physics, Ann Arbor, MI, USA. [6]Imperial College London, Physics Department, Blackett Laboratory, London, UK. [7]Department of Physics, University of Maryland, College Park, MD, USA. [8]STFC Rutherford Appleton Laboratory (RAL), Didcot, UK. [9]Department of Physics, Brown University, Providence, RI, USA. [10]Department of Physics, University of Zurich, Zurich, Switzerland. [11]Lawrence Berkeley National Laboratory (LBNL), Berkeley, CA, USA. [12]Department of Physics, University of Wisconsin-Madison, Madison, WI, USA. [13]Department of Physics, University of California, Berkeley, Berkeley, CA, USA. [14]School of Physics and Astronomy, University of Edinburgh, SUPA, Edinburgh, UK. [15]Department of Physics, University at Albany (SUNY), Albany, NY, USA. [16]Department of Physics, University of California, Davis, Davis, CA, USA. [17]Laboratório de Instrumentação e Física Experimental de Partículas (LIP), University of Coimbra, Coimbra, Portugal. [18]Department of Physics, University of Liverpool, Liverpool, UK. [19]Department of Physics, Pennsylvania State University, University Park, PA, USA. [20]Department of Physics, Royal Holloway, University of London, Egham, UK. [21]South Dakota School of Mines and Technology, Rapid City, SD, USA. [22]Department of Physics and Astronomy, University of Rochester, Rochester, NY, USA. [23]South Dakota Science and Technology Authority (SDSTA), Sanford Underground Research Facility, Lead, SD, USA. [24]Department of Physics & Astronomy, Northwestern University, Evanston, IL, USA. [25]Fermi National Accelerator Laboratory (FNAL), Batavia, IL, USA. [26]Department of Physics, University of Oxford, Oxford, UK. [27]Department of Physics, King's College London, London, UK. [28]University of Bristol, H.H. Wills Physics Laboratory, Bristol, UK. [29]School of Physics, The University of Sydney, Sydney, NSW, Australia. [30]Brookhaven National Laboratory (BNL), Upton, NY, USA. [31]Department of Physics, University of Massachusetts, Amherst, MA, USA. [32]Department of Physics & Astronomy, University of Alabama, Tuscaloosa, AL, USA. [33]Department of Physics & Astronomy, University of Califonia, Los Angeles, Los Angeles, CA, USA. [34]IBS Center for Underground Physics (CUP), Daejeon, South Korea. [35]Department of Physics and Astronomy, University of Sheffield, Sheffield, UK. [36]Department of Physics, University of Texas at Austin, Austin, TX, USA. [37]Lawrence Livermore National Laboratory (LLNL), Livermore, CA, USA. [38]Vatican Observatory, Vatican City, Italy. [39]School of Natural Sciences, Black Hills State University, Spearfish, SD, USA. [40]Department of Physics and Astronomy, Texas A&M University, College Station, TX, USA. [41]Present address: School of Physics, The University of Melbourne, Melbourne, VIC, Australia. ✉e-mail: bboxer@ucdavis.edu; sam.eriksen@bristol.ac.uk; yqie2@u.rochester.edu